

An ideal Weyl semimetal induced by magnetic exchange

J.-R. Soh,¹ F. de Juan,^{1,2,3} M. G. Vergniory,^{2,3} N. B. M. Schröter,⁴ M. C. Rahn,^{1,5} D. Y. Yan,⁶ M. Bristow,¹ P. A. Reiss,¹ J. N. Blandy,⁷ Y. F. Guo,^{8,9} Y. G. Shi,⁶ T. K. Kim,¹⁰ A. McCollam,¹¹ S. H. Simon,¹ Y. Chen,^{1,8} A. I. Coldea,¹ and A. T. Boothroyd^{1,*}

¹Department of Physics, University of Oxford, Clarendon Laboratory, Parks Road, Oxford OX1 3PU, UK

²Donostia International Physics Center, 20018 Donostia-San Sebastian, Spain

³IKERBASQUE, Basque Foundation for Science, Maria Diaz de Haro 3, 48013 Bilbao, Spain

⁴Paul Scherrer Institute, WSLA/202, 5232 Villigen PSI, Switzerland

⁵MPA-CMMS, Los Alamos National Laboratory, Los Alamos, New Mexico 87545, USA

⁶Beijing National Laboratory for Condensed Matter Physics,
Institute of Physics, Chinese Academy of Sciences, Beijing 100190, China

⁷Department of Chemistry, University of Oxford,
Inorganic Chemistry Laboratory, Oxford, OX1 3QR, UK

⁸School of Physical Science and Technology, ShanghaiTech University, Shanghai 201210, China

⁹CAS Center for Excellence in Superconducting Electronics (CENSE), Shanghai 200050, China

¹⁰Diamond Light Source, Harwell Campus, Didcot, OX11 0DE, UK

¹¹High Field Magnet Laboratory (HFML-EMFL),
Radboud University, 6525 ED Nijmegen, Nijmegen, Netherlands

(Dated: May 23, 2022)

Weyl semimetals exhibit exceptional quantum electronic transport due to the presence of topologically-protected band crossings called Weyl nodes^{1,2}. The nodes come in pairs with opposite chirality, but their number and location in momentum space is otherwise material specific. Following the initial discoveries^{3–5} there is now a need for better material realizations, ideally comprising a single pair of Weyl nodes located at or very close to the Fermi level and in an energy window free from other overlapping bands. Here we propose the layered intermetallic EuCd_2As_2 to be such a system^{6,7}. We show that Weyl nodes in EuCd_2As_2 are magnetically-induced via exchange coupling, emerging when the Eu spins are aligned by a small external magnetic field. The identification of EuCd_2As_2 as a model magnetic Weyl semimetal, evidenced here by *ab initio* calculations, photoemission spectroscopy, quantum oscillations and anomalous Hall transport measurements, opens the door to fundamental tests of Weyl physics.

I. INTRODUCTION

Weyl nodes are distinct from other topological features of electron band structures in several respects, including (1) the bulk bands that cross at a Weyl node are non-degenerate, (2) the associated Weyl fermions have a definite chirality, and (3) the Weyl nodes are protected against perturbations that do not couple the nodes^{1,2,8}. Moreover, the individual nodes within a pair act as a source and a sink of Berry curvature, a property which relates directly to the intrinsic anomalous Hall conductance and other physical phenomena^{1,9}.

Weyl semimetal (WSM) phases in crystals require either broken spatial inversion symmetry, or broken time-reversal symmetry (TRS), or both. There are a number of experimental realizations of the first type (with broken spatial inversion symmetry only), especially in the TaAs structural family^{3–5,10,11}, but magnetic WSMs (with broken TRS) are still rare. The few known candidates are complicated by multiple pairs of Weyl nodes and/or by extra (non-topological) Fermi surface pockets which shroud the Weyl nodes^{8,12–16}. The main advantage of magnetic WSMs for the purpose of exploring the basic properties of Weyl fermions is that systems with only two Weyl nodes are possible which, due to the inversion symmetry, are guaranteed to be at the same energy and so

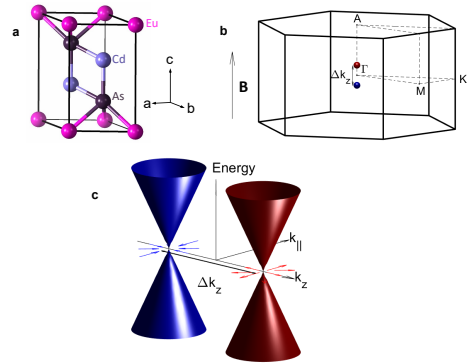


FIG. 1. Crystal structure of EuCd_2As_2 and location of Weyl nodes in the Brillouin zone. **a**, The trigonal unit cell for the space group $P\bar{3}m1$ (No. 164). The Weyl fermions predominantly occupy orbitals in the double-corrugated Cd_2As_2 layers, which are sandwiched between the Eu layers⁷. **b**, The Weyl nodes lie along the A– Γ –A high symmetry line and are separated by Δk_z (not shown to scale). **c**, In the fully polarized state, singly degenerate conduction and valence bands meet at a pair of Weyl nodes from which the bands disperse linearly. The nodes act as a source and sink of Berry curvature and have distinct chirality which depends on the direction of the field applied along the c axis.

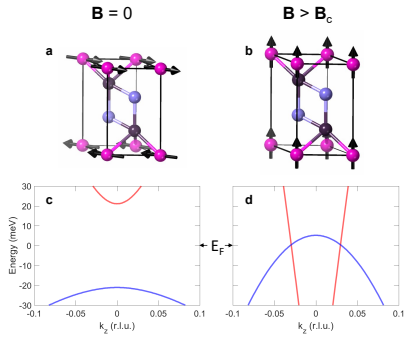


FIG. 2. Exchange-induced Weyl nodes in EuCd_2As_2 . **a,c** In zero field, the Eu spins order in an A-type antiferromagnetic structure at $T < T_N$, with the spins lying in the ab plane. The corresponding band structure is gapped at Γ . **b,d** The Eu moments can be fully polarized along the c axis in a small coercive field ($B > B_c$), lifting the double degeneracy of the bands and creating a pair of Weyl nodes along Γ –A, at $k_z = 0.03$ r.l.u.

have a vanishing density of states. WSMs formed by the breaking of inversion symmetry (but with TRS), by contrast, have a minimum of four nodes which are in general separated in energy.

We investigated bulk single crystals of EuCd_2As_2 (ECA), which has a trigonal crystal structure (Fig. 1a) containing alternating layers of Eu^{2+} and $[\text{Cd}_2\text{As}_2]^{2-}$ (ref. ¹⁷). The magnetization, magnetotransport and crystallographic parameters of our ECA crystals are fully consistent with earlier reports^{6,7,18} (see Methods and Supplementary Information). The europium ions carry a localized magnetic moment with spin $S = 7/2$ and zero orbital angular momentum. Below $T_N = 9.5$ K the spins order in an A-type antiferromagnetic (AFM) structure in which the spins are perpendicular to the crystallographic c axis and form ferromagnetic layers which stack antiferromagnetically along the c axis (Fig. 2a)⁷.

ECA is metallic at temperatures down to $T \sim 80$ K, but for lower temperatures the resistivity increases to a sharp maximum at T_N before falling again at lower temperatures. This behaviour has been interpreted as due to scattering of conduction electrons by localized Eu magnetic moments which are exchange-coupled to the Cd and As orbitals^{6,7}.

In previous *ab initio* electronic structure calculations, where spins in the AFM state were found to be aligned with the c axis, ECA was predicted to host a band inversion of doubly degenerate As $4p$ and Cd $5s$ states near the Fermi level (E_F), producing a crossing along the Γ –A line protected by C_3 symmetry^{7,19}. Experimentally⁷ (and in more recent calculations²⁰) the spins are in fact found to point perpendicular to the c axis (Fig. 2a) breaking C_3 symmetry, so an avoided crossing at finite momentum would be expected. In our new *ab initio* calculations, for a wide range of parameters, we find a small direct gap at

Γ instead, which is mostly insensitive to the orientation of the spins in the AFM state (Fig. 2c).

A relatively small magnetic field ($B_c = 1.6$ T at $T = 2$ K for $B \parallel c$) can be used to coerce the Eu spins into a fully aligned state⁷, and *ab initio* calculations for the ferromagnetic state, shown in Fig. 2b, are presented in Fig. 2d. When the Eu spins are fully spin-polarized along the c axis, the double degeneracy is lifted, and a single pair of Weyl nodes appears at E_F with no other Fermi surface pockets in the Brillouin zone. These Weyl nodes lie along the Γ –A high symmetry line (Fig. 1b) at wavevector $\vec{k} = (0, 0, k_0)$ with $k_0 \simeq \pm 0.03 \times 2\pi/c = \pm 0.26$ nm⁻¹. ECA in a small magnetic field, therefore, is predicted to be a Weyl semimetal, with a single pair of Weyl nodes located at E_F .

The band splitting in the saturated phase is ~ 100 meV, which is two orders of magnitude larger than the Zeeman splitting in the saturation field B_c . From this we can conclude, first, that the calculations, which include exchange but no Zeeman interaction, represent well the experiment when a small magnetic field is applied to polarize the Eu spins, and second, that the existence of the Weyl nodes is driven by exchange coupling to the Eu spins.

In order to validate the *ab initio* predictions we carried out angle-resolved photoemission spectroscopy (ARPES) and quantum oscillations measurements (see Methods). ARPES data on ECA for $T < T_N$ are presented in Fig. 3a,c.

These k – E plots are for k along the M– Γ –M path (see Fig. 1b) and show steeply dispersing bands approaching E_F . The spectra are in good agreement with the *ab initio* band structure (Figs. 3b and d) calculated for the observed AFM state with spins lying in the plane. The agreement is best when E_F is shifted slightly downward by about 50 meV, which indicates that the sample is very slightly hole-doped.

Our quantum oscillations measurements are summarized in Figs. 3e–g. Figure 3e shows the second derivative of the in-plane longitudinal resistance measured at $T = 1.4$ K in magnetic fields applied parallel to the c axis ($B \parallel c$) up to 37 T, well above the coercive field (see Supplementary Information for details of the data treatment). For $B < B_c$ there is a very strong variation in magnetoresistance associated with the progressive canting of the spins towards the c axis, shown also in Fig. 4a, but at higher fields the curve displays clear Shubnikov–de Haas (SdH) oscillations. Only a single SdH oscillation frequency could be resolved, consistent with a single band. Moreover, we do not find any evidence for a spin-splitting of the Landau levels, in contrast to the SdH data on the structurally-related Dirac semimetal Cd_3As_2 .²¹ A lack of spin splitting would be consistent with the prediction that for $B > B_c$ the bands are already split by a constant exchange field, implying that the observed SdH oscillations correspond to the small pockets derived from the Weyl points when E_F is shifted downwards slightly, as suggested by the ARPES measurements.

The maxima and minima of the oscillations are plot-

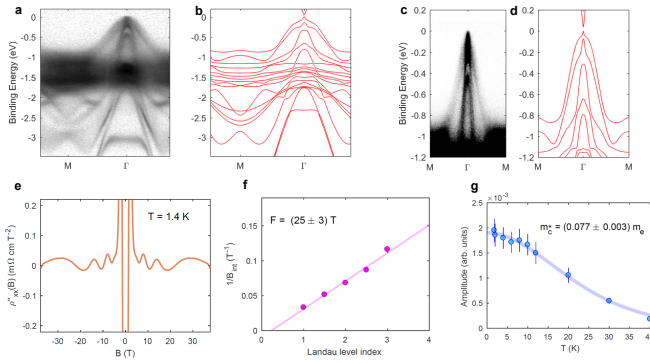


FIG. 3. ARPES and high-field magneto-transport of EuCd_2As_2 . **a, c**, ARPES spectrum as a function of wavevector along the $M-\Gamma-M$ high-symmetry line measured at $T \simeq 5$ K with incident photon energy of 130 eV. The data shown here are a sum of two measurements taken with linear-vertical and linear-horizontal polarization, respectively, to compensate the effect of selection-rules. Nonlinear scaling was applied to the intensity to enhance the visibility of bands with a small photoemission cross-section. **b, d**, Electronic bands calculated by DFT (in red). **e**, The second derivative of the longitudinal resistivity $\rho''_{xx}(B)$ as a function of field applied along the c axis. **f**, Plot of $1/B_{\text{int}}$ at the minima and maxima in ρ_{xx} against Landau level index, with integers assigned to the minima, where $B_{\text{int}} = B + \mu_0 M$ is the internal field. The SdH frequency F is obtained from the gradient of the linear fit shown. **g**, Temperature dependence of the amplitude in the SdH oscillation, measured at $B = 10$ T. The line is a fit to the Lifshitz-Kosevich formula, from which the cyclotron effective mass m_c^* of the charge carriers is estimated. The quoted error in m_c^* derives from the least-squares fit, but the uncertainty in the measurement is expected to be larger because of the long period of the oscillations and the relatively narrow field range.

ted on a Landau level index plot in Fig. 3f, with minima in ρ_{xx} assigned to the integers²². The SdH frequency obtained from the gradient is $F = 25 \pm 3$ T, which converts via the Onsager relation $F = (\hbar/2\pi e)A_{\text{ext}}$ to an extremal area of the Fermi surface perpendicular to the c axis of $A_{\text{ext}} = 0.24 \text{ nm}^{-2}$, or $k_F = 0.28 \text{ nm}^{-1}$ assuming a circular cross-section. Measurements at higher fields up to 45 T did not find any additional oscillation frequencies (see Supplementary Information), and confirmed that the maximum centred on 30 T in Fig. 3d corresponds to the quantum limit (first Landau level).

Figure 3f shows the temperature dependence of the SdH oscillation amplitude up to 40 K. By fitting the data to the Lifshitz-Kosevich formula (amplitude $\sim X/\sinh X$, where $X = 2\pi^2 k_B T m_c^* / e\hbar B$ and $m_c^* = (\hbar^2/2\pi) dA_{\text{ext}}/dE$) we obtain a cyclotron effective mass of about $m_c^* = 0.08 m_e$. The observation that $m_c^*/m_e \ll 1$ is consistent with quasiparticles near a Dirac or Weyl node. Our *ab initio* calculations also predict a light effective mass. Assuming $k_F = 0.28 \text{ nm}^{-1}$, as determined from the SdH data, and a circular Fermi surface cross-section, we obtain $m_c^* = 0.18 m_e$. We caution, however,

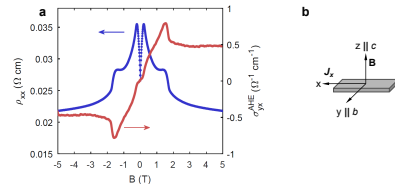


FIG. 4. Magneto-transport of EuCd_2As_2 . **a**, ρ_{xx} and σ_{yx} as a function of field. **b**, Definition of the xyz axes relative to the crystal orientation and directions of the current and applied field used in the measurement.

that the measured and calculated m_c^* are not directly comparable because the Lifshitz-Kosevich formula assumes that the Landau levels are equally-spaced and that many levels are filled, neither of which applies here.

Our quantum oscillations and ARPES results, as well as previous optical reflectivity measurements which found clear evidence for a very low carrier density⁶, all point to a very small Fermi surface, and support the prediction that in the spin-polarized state of ECA there is a single pair of Weyl nodes located close to Γ along $\Gamma-\text{A}$, in a small window of energy free from other bands. The small effective mass and Fermi surface area from the SdH data, together with *p*-type Hall transport⁷, indicate that the crystals used in this study are slightly hole-doped. From the SdH measurements and *ab initio* in-plane dispersion we estimate that E_F is located approximately 52 meV below the Weyl node, which is consistent with the shift applied to the DFT bands in order to match the ARPES data.

In recent years, there has been a great deal of interest in measuring anomalous transport effects caused by Berry curvature in topological semimetals, especially the anomalous Hall effect (AHE).^{9,23} In a Weyl semimetal, the Berry curvature is associated with the separation Δk of the Weyl nodes in \mathbf{k} -space, as illustrated in Fig. 1c, and for a single pair of nodes at E_F the anomalous Hall conductivity has the universal form⁹

$$\sigma_{yx}^{\text{AHE}} = \frac{e^2}{2\pi\hbar} \Delta k. \quad (1)$$

In experiments, Δk is typically field-dependent due to the effect of field on the band splitting. This makes it difficult to separate the anomalous and semi-classical contributions to the Hall effect, as the latter is also field-dependent. In ECA, however, Δk is almost constant for fields above the saturation field $B_c = 1.6$ T, which makes it straightforward to isolate the anomalous part of the Hall resistivity. In principle, therefore, ECA is an ideal system for studying the AHE experimentally.

Assuming $\Delta k \simeq 0.52 \text{ nm}^{-1}$ from our *ab initio* results, Eq. (1) predicts the anomalous Hall conductance for ECA to be $\sigma_{yx}^{\text{AHE}} \simeq 30 \Omega^{-1} \text{ cm}^{-1}$. This prediction, however, applies only when the Weyl nodes lie exactly at E_F . In the samples used here the nodes are slightly shifted in energy away from E_F , and in this situation other terms are expected to contribute to the AHE in addition to that from the Berry phase.²³ Bearing this in mind, we present in Fig. 4a measurements of the longitudinal magnetoresistance ρ_{xx} and the anomalous part of the transverse (Hall) conductivity σ_{yx}^{AHE} at $T = 2 \text{ K}$ as a function of field applied parallel to the c axis (the experimental geometry is shown in Fig 4b, and the procedure to obtain the anomalous part of σ_{yx} is described in the Supplementary Information). There are rapid changes in ρ_{xx} at low field due to the reorientation of the Eu spins in the magnetic field, as noted earlier, but above the saturation field $B_c = 1.6 \text{ T}$ ρ_{xx} decreases monotonically with field. The field range in Fig. 4a is below that where quantum oscillations become observable (see Fig. 3e). The $\sigma_{yx}^{\text{AHE}}(B)$ curve is an odd function of field, increasing from zero with field up to B_c and remaining constant for fields above B_c . The behaviour of $\sigma_{yx}^{\text{AHE}}(B)$ is consistent with a non-zero anomalous Hall conductivity, but the value of σ_{yx}^{AHE} for $B > B_c$ is significantly below that predicted by Eq. (1).

As well as the contribution from the Fermi surface in our samples, another factor which could be responsible for the reduction in σ_{yx}^{AHE} compared to the ideal case is disorder. We have found the AHE in ECA to be strongly reduced by the polishing process used to shape the Hall bar sample. Although it has been argued that disorder-induced contributions to the AHE are absent when E_F is near the nodes⁹, the presence of a tilt in the dispersion makes these contributions possible in the form of skew scattering^{24,25}. The significant tilt predicted in our *ab initio* calculations (Fig. 2d) might explain why the AHE is so reduced.

The simple structure of the Weyl nodes in ECA makes it an ideal material with which to study the different contributions to the AHE. This could be achieved by tuning the position of E_F relative to the Weyl nodes by doping or application of pressure, or by controlling the level of defects by irradiation. The degrading effects of polishing could be avoided by studying transport phenomena with thin film samples.

More generally, ECA could provide the means to test predictions of other exotic physics in Weyl semimetals, such as the anomalous Nernst and thermal Hall effects^{16,26}, non-reciprocal effects in light propagation²⁷, the repulsive Casimir effect²⁸, or to probe the effects of the chiral anomaly in the optical absorption²⁹ and non-local transport³⁰.

Methods: Single crystals of ECA were grown by the NaCl/KCl flux method described in ref.¹⁸. The structure and crystallographic quality of the single crystals were studied on a 6-circle x-ray κ diffractometer (Oxford Diffraction). To search for impurity phases, synchrotron x-ray powder diffraction measurements ($\lambda = 0.824678 \text{ \AA}$)

were performed on a crushed ECA crystal at the I11 beamline, Diamond Light Source (Didcot, UK).

Low-field ($\mu_0 H < 16 \text{ T}$) magneto-transport measurements were performed on a Physical Property Measurement System (Quantum Design) in a Hall configuration with the standard five-contact method. The longitudinal and Hall component were obtained by symmetrizing and anti-symmetrizing the data measured in the positive and negative fields, respectively (See Supplementary Information). High field in-plane resistivity measurements were performed at the High Field Magnet Laboratory (Nijmegen, Netherlands) using the 38 T resistive DC magnet.

We employed density functional theory (DFT) as implemented in the Vienna *Ab-initio* Simulation Package (VASP)^{31,32}. The exchange correlation term is described according to the Perdew-Burke-Ernzerhof (PBE) prescription together with projected augmented-wave pseudopotentials³³. For the self-consistent calculations we used a $10 \times 10 \times 5$ k-points mesh. The kinetic energy cut-off was set to 550 eV. The spin-polarized band structures are calculated within GGA+U, with the value of U chosen to be 5 eV. The lattice parameters used in the calculations were $a = b = 0.443 \text{ nm}$ and $c = 0.729 \text{ nm}$.

ARPES measurements were performed at the high-resolution branch line of the beamline I05 at the Diamond Light Source, UK³⁴. To compensate for the effect of selection rules that suppress the photoemission signal from certain bands under certain light polarizations, here we combined the intensities from two measurements taken at linear-vertical and linear-horizontal polarization (with respect to the sample normal). Measurements were performed with a Scienta R4000 analyzer at a photon energy of 130 eV, which approximately corresponds to the $k_z = \Gamma$ measurement plane, at a temperature of $T \sim 5 \text{ K}$.

ACKNOWLEDGMENTS

The research was supported by the U.K. Engineering and Physical Sciences Research Council (Grant Nos. EP/N034872/1, EP/M020517/1 and EP/N01930X/1). J.-R.S. acknowledges support from the Singapore National Science Scholarship, Agency for Science Technology and Research. F.d.J. acknowledges funding from the European Union's Horizon 2020 research and innovation programme under the Marie Skłodowska Curie grant agreement No. 705968. A.I.C. acknowledges support from an EPSRC Career Acceleration Fellowship (EP/I004475/1). M.C.R. is grateful to the Oxford University Clarendon Fund for the provision of a studentship, and to the Los Alamos National Laboratory Directors Fund and the Alexander von Humboldt-Stiftung for financial support. The crystal growth was carried out with support from the National Key Research and Development Program of China (grant nos. 2017YFA0302901 and 2016YFA0300604) and the Strategic Priority Research Program (B) of the Chinese Academy of Sciences

(Grant No. XDB07020100). We are grateful to the Oxford Centre for Applied Superconductivity and the Oxford University John Fell Fund for the provision of the 16 T PPMS. We thank the Diamond Light Source Ltd for the award of beam time on I11 (allocation EE18786) and I05 (allocation SI19234). The high magnetic field work was performed at the HFML-RU/FOM, a member of the European Magnetic Field Laboratory (EMFL), with additional support from the EPSRC (UK) via its membership of the EMFL (grant no. EP/N01085X/1), and at the National High Magnetic Field Laboratory, which is supported by National Science Foundation Cooperative Agreement No. DMR-1157490 and the State of Florida. We thank D. Graph for technical support during experiments using the 45 T hybrid magnet at the NHMFL, Tallahassee, USA.

Author contributions: F.d.J. and A.T.B. conceived the idea behind the experiments. J.-R.S., M.B.,

P.A.R., M.C.R. A.M. and A.I.C. carried out the magneto-transport measurements. The crystals were grown and characterised by D.Y.Y., Y.F.G. and Y.G.S. DFT calculations of the electronic band structure were performed by M.G.V. and J.-R.S., and additional input on theory was provided by S.H.S. ARPES measurements at beamline I05 of Diamond were made by N.B.M.S., J.-R.S. and T.K.K. The analysis of the ARPES data was carried out by N.B.M.S. Synchrotron powder diffraction measurements were performed at beamline I11 of Diamond by J.N.B. The manuscript was written by A.T.B., F.d.J. and J.R.S. All authors discussed the results and commented on the manuscript.

Competing Interests: The authors declare no competing interests.

Correspondence: Correspondence and requests for materials should be addressed to A.T.B.

* andrew.boothroyd@physics.ox.ac.uk

- ¹ Armitage, N. P., Mele, E. J., Vishwanath, A. Weyl and Dirac semimetals in three-dimensional solids. *Rev. Mod. Phys.* **90**, 015001 (2018).
- ² Burkov, A. A. Topological semimetals. *Nature Materials* **15**, 1145–1148 (2016).
- ³ Xu, S.-Y. *et al.* Discovery of a Weyl fermion semimetal and topological Fermi arcs. *Science* **349**, 613–617 (2015).
- ⁴ Lv, B. Q. *et al.* Observation of Weyl nodes in TaAs *Nature Phys.* **11**, 724–728 (2015).
- ⁵ Yang, L. X. *et al.* Weyl semimetal phase in the non-centrosymmetric compound TaAs *Nature Phys.* **11**, 728–733 (2015).
- ⁶ Wang, H. P., Wu, D. S., Shi, Y. G., & Wang, N. L. Anisotropic transport and optical spectroscopy study on antiferromagnetic triangular lattice EuCd₂As₂: An interplay between magnetism and charge transport properties. *Phys. Rev. B* **94**, 045112 (2016).
- ⁷ Rahn, M. C. *et al.* Coupling of magnetic order and charge transport in the candidate Dirac semimetal EuCd₂As₂. *Phys. Rev. B* **97**, 214422 (2018).
- ⁸ Wan, X., Turner, A. M., Vishwanath A. & Savrasov, S. Y. Topological semimetal and Fermi-arc surface states in the electronic structure of pyrochlore iridates. *Phys. Rev. B* **83**, 205101 (2011).
- ⁹ Burkov, A. A. Anomalous Hall Effect in Weyl Metals. *Phys. Rev. Lett.* **113**, 187202 (2014).
- ¹⁰ Xu, S.-Y. *et al.* Discovery of a Weyl fermion state with Fermi arcs in niobium arsenide. *Nature Phys.* **11**, 748–755 (2015).
- ¹¹ Xu, S.-Y. *et al.* Experimental discovery of a topological Weyl semimetal state in TaP. *Sci. Adv.* **1**, e1501092 (2015).
- ¹² Suzuki, T. *et al.* Large anomalous Hall effect in a half-Heusler antiferromagnet. *Nat. Phys.* **12**, 1119–1123 (2016).
- ¹³ Liu, E. *et al.* Giant anomalous Hall effect in a ferromagnetic kagome-lattice semimetal. *Nat. Phys.* **14**, 1125–1131 (2018).
- ¹⁴ Wang, Z. *et al.* Time-reversal-breaking Weyl fermions in magnetic Heusler alloys. *Phys. Rev. Lett.* **117**, 236401 (2016).
- ¹⁵ Nakatsuji, S., Kiyohara, N. & Higo, T. Large anomalous Hall effect in a non-collinear antiferromagnet at room temperature. *Nature* **527**, 212–215 (2015).
- ¹⁶ Sakai, A. *et al.* Giant anomalous Nernst effect and quantum critical scaling in a ferromagnetic semimetal. *Nat. Phys.* **14**, 1119–1124 (2018).
- ¹⁷ Artmann, A., Mewis, A., Roepke, M., & Michels, G. *AM₂X₂-Verbindungen mit CaAl₂Si₂-Struktur. XI [1] Struktur und Eigenschaften der Verbindungen ACd₂X₂ (A: Eu, Yb; X: P, As, Sb).* *Z. Anorg. Allg. Chem.* **622**, 679–682 (1996).
- ¹⁸ Schellenberg, I., Pfannenschmidt, U., Eul, M., Schwickerdt, C. & Pöttgen, R. A ¹²¹Sb and ¹⁵¹Eu Mössbauer Spectroscopic Investigation of EuCd₂X₂ (X = P, As, Sb) and YbCd₂Sb₂. *Z. Anorg. Allg. Chem.* **637**, 1863–1870 (2011).
- ¹⁹ Hua, G. *et al.* Dirac semimetal in type IV magnetic space groups. *Phys. Rev. B* **98**, 201116(R) (2018).
- ²⁰ Krishna, J., Nautiyal, T. & Maitra, T. First-principles study of electronic structure, transport, and optical properties of EuCd₂As₂. *Phys. Rev. B* **98**, 125110 (2018).
- ²¹ Narayanan, A., *et al.* Linear magnetoresistance caused by mobility fluctuations in *n*-doped Cd₃As₂. *Phys. Rev. Lett.* **114**, 117201 (2015).
- ²² Ando, Y. Topological Insulator Materials. *J. Phys. Soc. Jpn.* **82**, 102001 (2013).
- ²³ Nagaosa, N., Sinova, J., Onoda, S., MacDonald, A. H. & Ong, N. P. Anomalous Hall effect. *Rev. Mod. Phys.* **82**, 1539–1592 (2010).
- ²⁴ Steiner, J. F., Andreev, A. V. & Pesin, D. A. Anomalous Hall effect in type-I Weyl metals. *Phys. Rev. Lett.* **119**, 036601 (2017).
- ²⁵ Mukherjee, S. P. & Carbotte, J. P. Anomalous DC Hall response in noncentrosymmetric tilted Weyl semimetals. *J. Phys.: Condens. Matter* **30**, 115702 (2018).
- ²⁶ Ferreiros, Y., Zyuzin, A. A. & Bardarson, J. H. Anomalous Nernst and thermal Hall effects in tilted Weyl semimetals. *Phys. Rev. B* **96**, 115202 (2017).
- ²⁷ Kotov, O. V. and Lozovik, Y. E. Giant tunable nonreciprocity of light in Weyl semimetals. *Phys. Rev. B* **98**, 195446 (2018).

- ²⁸ Wilson, J. H., Allocca, A. A. and Galitski, V. Repulsive Casimir force between Weyl semimetals. *Phys. Rev. B* **91**, 235115 (2015).
- ²⁹ Ashby, P. E. C. & Carbotte, J. P. Chiral anomaly and optical absorption in Weyl semimetals. *Phys. Rev. B* **89**, 245121 (2014).
- ³⁰ Parameswaran, S. A., Grover, T., Abanin, D. A., Pesin, D. A. & Vishwanath, A. Probing the chiral anomaly with non-local transport in three-dimensional topological semimetals. *Phys. Rev. X* **4**, 031035 (2014).
- ³¹ Kresse, G. & Furthmüller, J. Efficiency of *ab-initio* total energy calculations for metals and semiconductors using a plane-wave basis set. *Comp. Mater. Sci.* **6**, 15 (1996).
- ³² Kresse, G. & Furthmüller, J. Efficient iterative schemes for *ab-initio* total-energy calculations using a plane-wave basis set. *Phys. Rev. B* **54**, 11169 (1996).
- ³³ Perdew, J. P., Burke, K. & Ernzerhof, M. Generalized Gradient Approximation Made Simple. *Phys. Rev. Lett.* **77**, 3865 (1996).
- ³⁴ Hoesch, M. *et al.* A facility for the analysis of the electronic structures of solids and their surfaces by synchrotron radiation photoelectron spectroscopy. *Rev. Sci. Instrum.* **88**, 013106 (2017).